sion plaques, and activation/deactivation of Rho family (Rho, Rac1, and Cdc42) occur simultaneously with culture time. Before the discussion of the Rho activity-cell shape/motility relationship, the experimental results are summarized as follows.

- Adhesion potential: at 3 h, the number of adhered cells was almost identical for both TCPS and PET, whereas that for PS was very small. At 24 h, there was no significant difference in the number of adhered cells among the three substrates.
- Cell shape and morphology: at 3 h, the subpopulation of spread cells was the highest on TCPS, followed by that on PET. Minimal population was noticed on PS, and concomitantly the subpopulation of round (or nonspread) cells was the highest for PS, followed by that for PET, and lastly, that for TCPS. The population of cells with lamellipodia was almost the same at 3 h after plating and increased thereafter irrespective of the type of substrate used. There was some substrate-dependent difference in population at 24 h. The lowest cell population was found for PS.
- Cell motility: the average speed of cell movement was not significantly different among cells on the three types of substrates and the observation periods. However, the length of final displacement, the average rate of displacement, and the coefficient of dislocation efficacy increased at the later period of observation for all substrates. These three parameters were highest for PS, regardless of the observation period.
- Activation of Rho family: Rho activation was maximal at 0.5–1.0 h after plating and gradually decreased thereafter to reach the basal level, irrespective of the type of substrate used. Almost the same level of Rac1 activation was noted during the entire observation period for cells on TCPS and PET (approximately 1.5-fold higher than the basal level), whereas for cells on PS, a maximal level was observed at 0.5 h after plating and continuously decreased to the basal level thereafter. The continuous Cdc42 activation occurred for each substrate, but the degree of activation was the highest for cells on TCPS, followed by those on PET. Minimal activation was found for cells on PS.

From these results, we postulate the following interrelationships between temporal cell shape/morphology/migration and activation of Rho family. Strong adhesivity and rapid spreading, both of which were observed in cells on PET and TCPS, should be caused by the strong interaction between integrin and substrate (via adsorbed protein), which is related to the continuously constant activation of Rac1 and Cdc42. The least adhesive substrate, PS, probably because of the weakest interaction between integrin and proteins on the substrate, continuously decreased Rac1 activation and exhibited very small activation of Cdc42. This may be responsible for the retarded spreading. As for cell motility, cells on PS, the least adhesive substrate, appeared to exhibit the highest motility. Although the formation of pseudopods including lamellipodia and filopodia is required for cell motility, small levels of activation of Rac1 and Cdc42 appear to be beneficial for cell motility because the less spreading cells have lower interaction strength with the substrate. Much literature reported that Rac1 activity enhances cell raffling or microscopic, regional movement at the peripheral region (lamellipodia) of cells. Therefore, we expected that there must be some correlation between motility and Rac1 activity. However, the present study did not provide any correlation. Although we have little rational interpretation on this matter, one possible interpretation is that macroscopic cell movement requires the locomotion of a whole body of cells to which raffling is only partly contributed.

As for the substrate-induced Rho activation, McClay and Grainger[26] first reported in-depth study using two well-defined substrates: one is carboxyl group terminus-bearing self-assembled monolayer (SAM) on gold substrate, and the other is methyl group terminus-bearing SAM, both of which were prepared using corresponding alkanethiol. Their study was focused to activation of Rho-A, which is primarily known for its regulation of cell-surface-induced focal contact and stress fiber formation upon Rho-A-stimulated bundling and contractility of actin-myosin complexes leading to the clustering of integrin receptors. Their findings include that carboxyl group-terminated SAM, on which Swiss 3T3 fibroblasts spread well, enhanced Rho-A activation more than methyl group-terminated SAM, which is a less adherent substrate than the former SAM, whereas the nonactivated GDI-Rho level was much higher for the methyl group-terminated SAM than the carboxyl group-terminated SAM. These results support that surface chemistry greatly influences the activation state of Rho-A. Koenig et al.[27] tried to correlate cell adhesion with Rho-A. Rho-A activation in the nearly confluent, quiescent, nondividing cells on TCPS likely was minimal, whereas the less-adherent Teflon (polytetrafluoroethylene) surface exhibited the highest Rho-A activation, suggesting that survival activity of cells appears to enhance Rho-A activity.[27] The other relating preceding study by Putnam et al.,[28] includes externally applied mechanical forces-dependent activation of membrane-associated Rho-A and Rac: the activation of Rho-A and Rac is increased under compression strain but is decreased under tensile strain,[28] affecting the change in the state of microtubule polymerization. To our knowledge, besides these studies, there is no report to

establish the substrate-dependent relationship between cellular behaviors (cell shape, cell morphology, cytoskeletal architecture, and cell motility) and the activation of the Rho family, which has been recently identified as central coordinators of a remarkable variety of cell functions, as mentioned above. Although a clear-cut relationship between Rho and cell behaviors was not established in this study, the accumulation of more data may define the degree of contribution of Rho activation to these cellular behaviors, which will determine tissue compatibility, tissue morphogenesis, and engineered tissue architecture, all of which are the fundamental basis of artificial implants and tissue engineered devices.[1-4]

References

1. Saltzman WM. Cell interactions with polymers: principles of tissue engineering. Lanze RP, Langer R, Chick WL, editors. San Diego: Academic Press; 1997. p 225.
2. Lackie JM. Cell movement and cell behaviour. London: Allen & Unwin; 1986.
3. Ross JM. Cell–extracellular matrix interactions. In: Patrick CW Jr, Mikos AG, McIntire LV, editors. Frontiers in tissue engineering. Elmsford, NY: Pergamon; 1998.
4. Al-Rubeai M. Cell engineering. Boston: Kluwer Academic Publishers; 1999.
5. Burridge K, Chrzanowska-Wodnicka M. Focal adhesions, contractility, and signaling. Annu Rev Cell Dev Biol 1996;12:463–519.
6. Hall A. Rho GTPases and the actin cytoskeleton. Science 1998; 279(5350):509–514.
7. Schwartz MA, Shattil SJ. Signaling networks linking integrins and rho family GTPases. Trends Biochem Sci 2000;25(8):388–391.
8. Schmitz AA, Govek EE, Bottner B, Van Aelst L. Rho GTPases: signaling, migration, and invasion. Exp Cell Res 2000;261(1):1–12.
9. Zheng Y, Olson MF, Hall A, Cerione RA, Toksoz D. Direct involvement of the small GTP-binding protein Rho in lbc oncogene function. J Biol Chem 1995;270(16):9031–9034.
10. Ridley AJ, Hall A. The small GTP-binding protein rho regulates the assembly of focal adhesions and actin stress fibers in response to growth factors. Cell 1992;70(3):389–399.
11. Hartwig JH, Bokoch GM, Carpenter CL, Janmey PA, Taylor LA, Toker A, Stossel TP. Thrombin receptor ligation and activated Rac uncap actin filament barbed ends through phosphoinositide synthesis in permeabilized human platelets. Cell 1995;82(4):643–653.
12. Ridley AJ, Paterson HF, Johnston CL, Diekmann D, Hall A. The small GTP-binding protein rac regulates growth factor-induced membrane ruffling. Cell 1992;70(3):401–410.
13. Kozma R, Ahmed S, Best A, Lim L. The Ras-related protein Cdc42Hs and bradykinin promote formation of peripheral actin microspikes and filopodia in Swiss 3T3 fibroblasts. Mol Cell Biol 1995;15(4):1942–1952.
14. Symons M, Derry JM, Karlak B, Jiang S, Lemahieu V, Mccormick F, Francke U, Abo A. Wiskott-Aldrich syndrome protein, a novel effector for the GTPase CDC42Hs, is implicated in actin polymerization. Cell 1996;84(5):723–734.
15. Nobes CD, Hall A. Rho, rac, and cdc42 GTPases regulate the assembly of multimolecular focal complexes associated with actin stress fibers, lamellipodia, and filopodia. Cell 1995;81(1): 53–62.
16. Machesky LM, Hall A. Rho: a connection between membrane receptor signaling and the cytoskeleton. Trends Cell Biol 1996; 6:304–310.
17. Zamir E, Geiger B. Molecular complexity and dynamics of cell-matrix adhesions. J Cell Sci 2001;114:3583–3590.
18. Ren XD, Kiosses WB, Schwartz MA. Regulation of the small GTP-binding protein Rho by cell adhesion and the cytoskeleton. EMBO J 1999;18(3):578–585.
19. Paddock SW, Dunn GA. Analysing collisions between fibroblasts and fibrosarcoma cells: fibrosarcoma cells show an active invasionary response. J Cell Sci 1986;81:163–187.
20. Nishimura KY, Isseroff RR, Nuccitelli R. Human keratinocytes migrate to the negative pole in direct current electric fields comparable to those measured in mammalian wounds. J Cell Sci 1996;109:199–207.
21. Boudreau N, Bissell MJ. Extracellular matrix signaling: integration of form and function in normal and malignant cells. Curr Opin Cell Biol 1998;10:540–646.
22. Gumbiner BM. Cell adhesion: the molecular basis of tissue architecture and morphogenesis. Cell 1996;84:345–357.
23. Settleman J. Getting in shape with Rho. Nat Cell Biol 2000;2: E7–E9.
24. Small JV, Kaverina I, Krylyshkina O, Rottner K. Cytoskeleton cross-talk during cell motility. FEBS Lett 1999;452:96–99.
25. Kaverina I, Krylyshkina O, Small JV. Regulation of substrate adhesion dynamics during cell motility. Int J Biochem Cell Biol 2002;34:746–761.
26. McClay KB, Grainger DW. Rho-A–induced changes in fibroblasts cultured on organic monolayers. Biomaterials 1999;20: 2435–2446.
27. Koenig AL, Gambillava V, Grainger DW. Correlating fibronectin adsorption with endothelial cell adhesion and signaling on polymer substrates. J Biomed Mater Res 2002;64A:20–37.
28. Putnam AJ, Cunningham JJ, Pillemer BB, Mooney DJ. External mechanical strain regulates membrane targeting of Rho GTPases by controlling the state of microtubule polymerization. Am J Physiol Cell Physiol 2003;284:C627–639.

Confocal imaging of biofilm formation process using fluoroprobed *Escherichia coli* and fluoro-stained exopolysaccharide

Ryo Maeyama,[1,2] Yoshimitsu Mizunoe,[3] James M. Anderson,[4] Masao Tanaka,[2] Takehisa Matsuda[1]
[1]*Department of Biomedical Engineering, Faculty of Medical Sciences, Kyushu University, Maidashi, Fukuoka 812-8582, Japan*
[2]*Department of Surgery and Oncology, Faculty of Medical Sciences, Kyushu University, Maidashi, Fukuoka 812-8582, Japan*
[3]*Department of Bacteriology, Faculty of Medical Sciences, Kyushu University, Maidashi, Fukuoka 812-8582, Japan*
[4]*Department of Pathology, Case Western Reserve University, 2085, Adelbert Road, Cleveland, Ohio 44106-4907*

Received 5 March 2004; revised 17 March 2004; accepted 19 March 2004
Published online 4 June 2004 in Wiley InterScience (www.interscience.wiley.com). DOI: 10.1002/jbm.a.30077

Abstract: We developed a novel method of evaluating biofilm architecture on a synthetic material using green fluorescent protein-expressing *Escherichia coli* and red fluorescence staining of exopolysaccharides. Confocal laser scanning microscopy observation revealed the time course of the change in the *in situ* three-dimensional structural features of biofilm on a polyurethane film without structural destruction: initially adhered cells are grown to form cellular aggregates and secrete exopolysaccharides. These cells were spottily distributed on the surface at an early incubation time but fused to form a vertically grown biofilm with incubation time. Fluorescence intensity, which is a measure of the number of cells, determined using a fluorometer and biofilm thickness determined from confocal laser scanning microscopy vertical images were found to be effective for quantification of time-dependent growth of biofilms. The curli (surface-located fibers specifically binding to fibronectin and laminin)-producing *Escherichia coli* strain, YMel, significantly proliferated on fibronectin-coated polyurethane, whereas the curli-deficient isogenic mutant, YMel-1, did not. The understanding of biofilm architecture in molecular and morphological events and new fluorescence microscopic techniques may help in the logical surface design of biomaterials with a high antibacterial potential. © 2004 Wiley Periodicals, Inc. J Biomed Mater Res 70A: 274–282, 2004

Key words: biofilm; green fluorescent protein; confocal laser scanning microscopy; *Escherichia coli*; curli

INTRODUCTION

The biomass of bacteria and extracellular materials including exopolysaccharides (EPS) that accumulate on synthetic substrates is called a biofilm.[1,2] Once a biofilm is formed on artificial implants in the body, serious, often life-threatening events or situations such as "septic shock," defined as a systemic response to infection, occur, which cannot be managed by antimicrobial drug administration due to a high level of resistance to drug diffusion into the well-stabilized biofilm bioarchitecture.[3] Implanted artificial prostheses, which are often associated with biomaterial-based biofilms, include cardiovascular implants, orthopedic replacements, intraocular implants, and intravascular catheters. Biliary stents and urinary catheters are often occluded by biofilms of *Escherichia coli*, resulting in complications in patients.[4] For cardiovascular implants, a second surgery to replace a bacterial-infected implant with a new one is often necessary.

The microbial colonization, and the nature and architecture of biofilms on synthetic polymers have been studied over a few decades. Previous studies have revealed various aspects of biofilms qualitatively as well as quantitatively, particularly focusing on adhered and proliferated cells by microscopy, plate counting, or dye-staining technique.[5–8] Electron microscopy has been used to observe the three-dimen-

Correspondence to: T. Matsuda; e-mail: matsuda@med.kyushu-u.ac.jp
Contract grant sponsor: Ministry of Health, Labour and Welfare (MHLW) of Japan, Grant-in-Aid for Scientific Research
Contract grant sponsor: Ministry of Education, Culture, Sports, Science, and Technology (MEXT) of Japan, Grant-in-Aid for Scientific Research and for the Creation of Innovations through Business-Academic-Public Sector Cooperation
Contract grant sponsor: NIH/NIBIB; contract grant number: EB-00279

sional (3D) structural features of biofilms.[9] However, this method often destroys biofilms because of complicated fixation procedures such as dehydration and fails to show an "as-is" structure.[10] Therefore, the formation of an as-is 3D structure of a biofilm of *E. coli* on synthetic polymers has not yet been fully understood.

Confocal laser scanning microscopy (CLSM) enables the high-resolution fluorescence imaging and deep optical sectioning of biological structures with negligible background interface. Additionally, CLSM enables a biofilm to be observed under hydrated conditions, thus maintaining an as-is structure without structure destruction.[11] When combined with fluorescent probes, CLSM can be effectively used for the visualization of biofilm components. In recent years, green fluorescent protein (GFP) from jellyfish *Aequorea victoria* has emerged as an *in situ* marker of living cells. EPS, which are produced by *E. coli* and which serve as structural anchors for bacterial cells in biofilms, can be specifically stained with a fluorescent dye, rhodamine-labeled lectin.[12,13] The co-use of GFP-expressing *E. coli* and rhodamine-labeled lectin under CLSM enables us to obtain in-depth information on the distribution state of the bacterial and EPS components of 3D biofilms.

The objective of this study was to perform an *in situ* visualization of the 3D structure of *E. coli*–based biofilm on polyurethane (PU) films. *In situ* monitoring using the CLSM technique enabled us to analyze the time-dependent construction of 3D-structured biofilms on a synthetic polymer. Two *E. coli* strains, curli-producing (YMel) and curli-deficient (YMel-1), were used.[14,15] Curli are surface organelles of *E. coli*, which are composed of thin fibers with a diameter of approximately 2 nm that mediate binding to adhesive proteins specific to fibronectin and laminin found in the eucaryotic extracellular matrix.[16] The significant role of curli in biofilm formation on a fibronectin-precoated substrate was clearly demonstrated.

MATERIALS AND METHODS

Bacterial strains and plasmid

The *E. coli* strains used in this study were the curli-producing strain YMel and the curli-deficient isogenic mutant strain YMel-1, both of which were transformed by electroporation with the *gfp*mut3* gene encoding plasmid DNA (pJBA27) and expressing a stable green fluorescent protein (Gfpmut3*) as previously reported.[17] *E. coli* from the frozen bacterial solution was cultured in 3 mL of modified Luria-Bertani medium containing 50 μg/mL ampicillin and 3 g/L NaCl at 37°C for 18 h under aerobic conditions, and then scaled up to a concentration of approximately 2×10^8 colony forming units per milliliter (CFU/mL), which was determined by the plate count method. Then they were diluted to a concentration of 2×10^5 CFU/mL, which was used as an initial concentration for experiments.

CLSM

The biofilms were examined by CLSM (Radiance 2000; BioRad, Hercules, CA). Square PU sheets (obtained from Olympus Optical Co., Ltd., Tokyo, Japan), which were cut to fit a six-well cell culture cluster, were sterilized using ethylene oxide, placed in a six-well cell culture cluster using sterilized forceps, and incubated with *E. coli* cell suspension (2×10^5 CFU/mL) under static condition. After 3-, 6-, 12-, and 24-h incubations, culture medium was removed and phosphate-buffered saline (PBS) was gently added to prevent drying of the biofilms. To visualize the EPS of the biofilms, rhodamine-labeled concanavalin A (5 μg/mL; Vector Laboratories, Burlingame, CA), which specifically binds to D-(+)-glucose and D-(+)-mannose groups on EPS, was used. One hundred microliters of this fluorescent solution was carefully applied on top of the biofilms grown on the PU sheet. After a 30-min incubation in the dark at room temperature, the excess staining solution was removed by four rinses with PBS. Images were recorded at an excitation wavelength of 488 nm and an emission wavelength of 515 ± 30 nm for GFP and at an excitation wavelength of 514 nm and an emission wavelength of 600 ± 50 nm for rhodamine-labeled concanavalin A.

Electron microscopy

For negative staining, *E. coli* cells, harvested from the biofilm formed on the PU sheet after a 24-h incubation, were mixed with distilled water, and the suspension was allowed to sediment for 2 min on a grid. After washing with distilled water, the specimen was negatively stained with 2% uranyl formiate and air dried before transmission electron microscopy (H-7000E; Hitachi, Tokyo, Japan).

For scanning electron microscopy (SEM), the biofilm grown on a glass slide (Matsunami Glass Industries Ltd., Osaka, Japan) after a 24-hr incubation was fixed in 2% glutaraldehyde (Electron Microscopy Sciences, Hatfield, PA) in 0.1*M* phosphate buffer for 1 h at room temperature. The fixed samples were dehydrated for 20 min at each step in an ascending acetone series, sputter-coated with platinum, and evaluated by SEM (JSM-840A; JEOL, Tokyo, Japan).

Bacterial adhesion study

The adhesion of bacteria was studied under static condition. Round PU sample sheets sterilized by ethylene oxide were placed in a 24-well cell culture cluster using sterilized forceps and incubated with *E. coli*. After 3-, 6-, 12-, and 24-h incubations, the round PU sheets were rinsed with PBS,

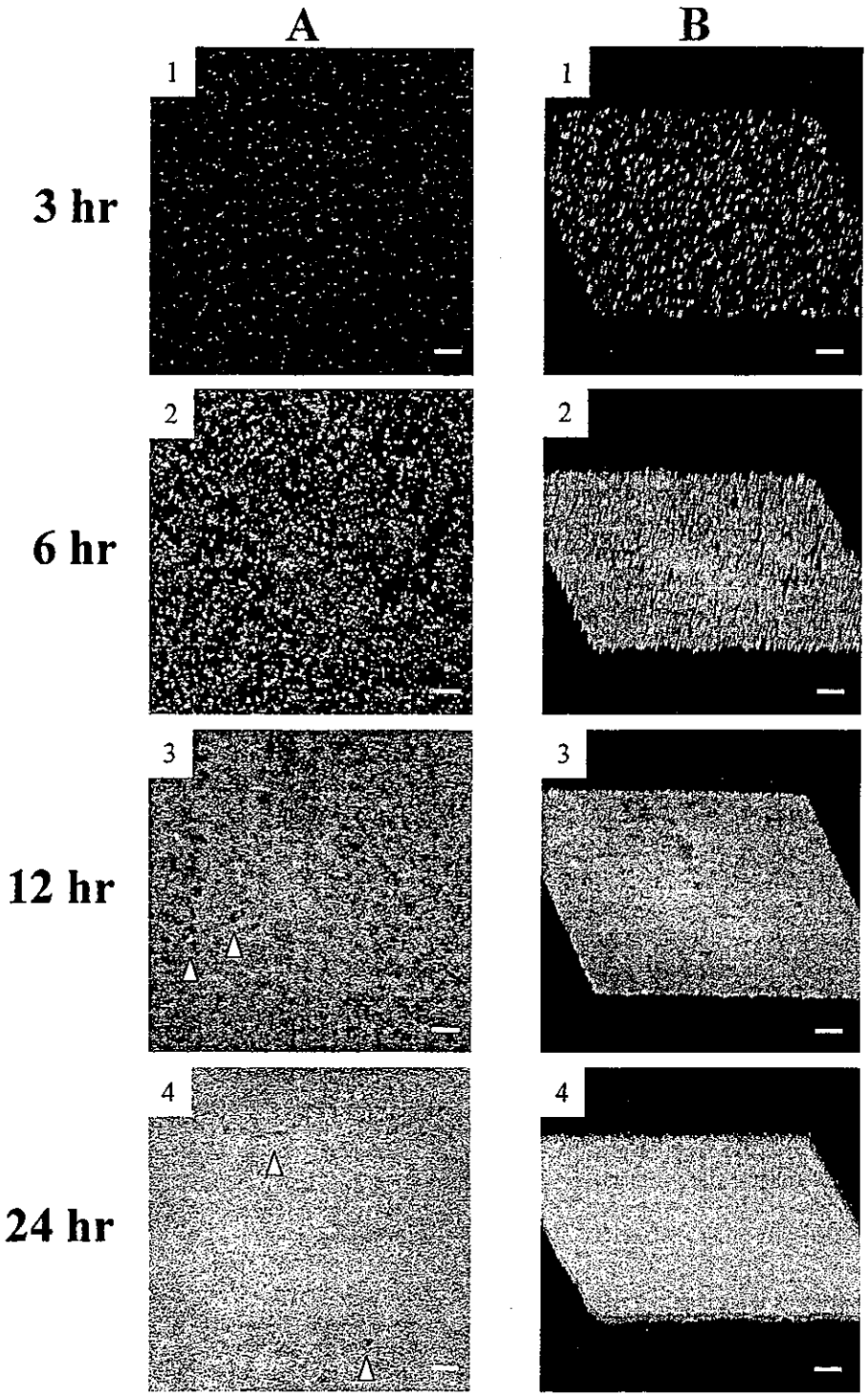

Figure 1. CLSM photographs of biofilms on PU at 3, 6, 12, and 24 h of incubations. (A) top view; (B) oblique view. Bar: 100 μm. Green and red areas indicate *E. coli* (expressing GFP) and EPS (stained with rhodamine-labeled concanavalin A), respectively. Irregular dark spots indicate water channels (white arrowheads).

placed in 15-mL Eppendorf tubes with 2 mL of PBS and sonicated for 60 s. Complete detachment of bacterial cells from the round sheets after 60-s sonication was confirmed by CLSM. Then, 100 μL of the solution containing detached bacterial cells was placed in a 96-well cell culture cluster and fluorescence intensity was measured with Molecular Imager FX (BioRad). Viable bacterial cells (CFU/cm^2) were also counted by the plate count method. Experiments were run with five samples, and the mean and standard deviation were recorded.

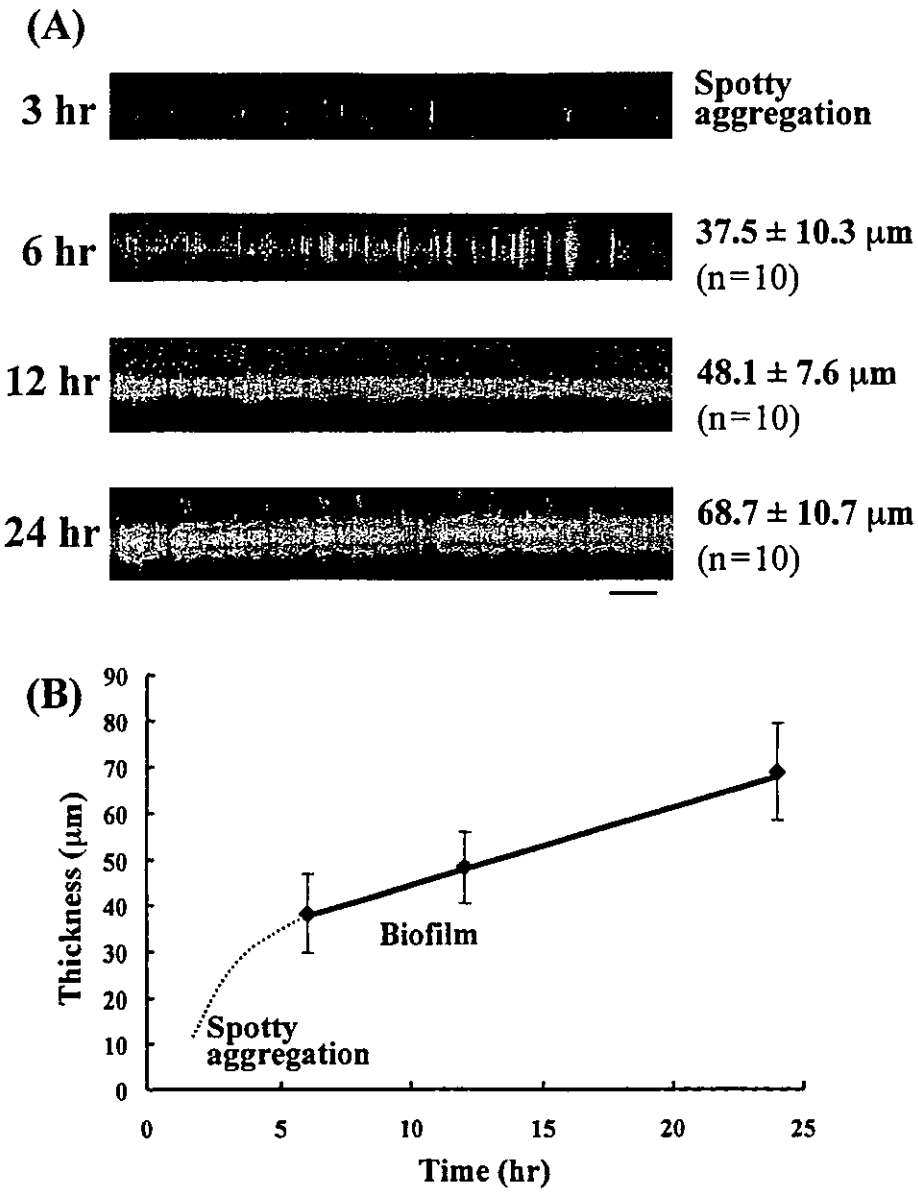

Figure 2. (A) CLSM photographs of vertical section of biofilms on PU at 3, 6, 12, and 24 h of incubations. Bar: 100 μm. (B) Biofilm thickness was determined by measuring the present images at 3, 6, 12, and 24 h of incubations. Ten vertical lines were randomly chosen for the analysis of each image. Values are expressed as means ± SD.

Protein coating of materials

Round PU sheets were incubated with bovine fibronectin (Itoham Foods Inc., Hyogo, Japan), bovine vitronectin (Yagai Co., Yamagata, Japan), and bovine serum albumin (Itoham Foods) at 1 mg/mL (0.1%) at 37°C for 24 h. Then, Luria-Bertani medium containing *E. coli* (2×10^5 CFU/mL) was poured over the protein-precoated round PU sheets and adherence was examined.

Statistical analysis

Statistical analysis was performed with the StatView 5.0 program (Abacus, Berkeley, CA). Data are shown as means ± SD. Statistical analysis was performed by analysis of variance. Differences at $p < 0.05$ were considered significant.

RESULTS

CLSM observation

To observe the 3D structure of the biofilm formed on the PU film, GFP-expressing YMel was cultured on the substrate under static condition for up to 24 h. After gentle washing with PBS, EPS generated during

biofilm formation was stained with rhodamine-labeled concanavalin A. The biofilm was observed using CLSM with time. Figure 1 shows (A) top-view and (B) oblique-view images of biofilms. At 3 h of incubation, adhered YMel cells (green color) randomly distributed without aggregate formation, and the EPS (red) formed regionally exhibited a thin cloudlike structure. At 6 h of incubation, the number of adhered YMel cells increased to form heterogeneous mosaic colonies composed of small aggregates that are scattered all over the substrate, and high-intensity red EPS regions tended to enlarge to cover the majority of the surface, thus initiating the formation of 3D structural constructs. The coexisting regions composed of green cells and red EPS were observed as a yellow region [Fig. 1(2B)]. At 12 h of incubation, the surface was completely covered with green (a major continuous matrix phase), yellow, and some spotty red regions (a dispersed domain). A small number of irregular dark spots were observed, which are supposed to be water channels, as described in the Discussion section. At 24 h of incubation, almost the entire surface area was yellowish-green, and the oblique-view CLSM image suggests that a thick biofilm was formed.

Figure 2(A) shows the time-lapse images of the vertical sections of biofilms. At the initial phase, spotty aggregates and single cells, which scattered horizontally but elongated vertically, were observed. At 6 h of incubation, the number of aggregates increased horizontally and formed a filmlike structure which enabled thickness measurement. At 12 h of incubation, the biofilm appeared more tightly packed. At 24 h of incubation, the vertical cross-sectional image revealed that EPS (yellow area) are predominantly located in the midlayer of the biofilm. To examine change in thickness with time, 10 vertical lines were randomly chosen for the measurement on each image for 6-, 12-, and 24-h incubations. Figure 2(B) shows that the average thickness of biofilms gradually increased with incubation time within the experimentally observed period.

Electron microscopic observation

The biofilm grown on glass for 24 h was observed using SEM. Figure 3 shows that *E. coli* and EPS, the matrix of the biofilm, formed a complex 3D structure. Irregularly shaped spaces resembling water channels were observed among dense structures. To confirm the expression of curli, which specifically bind to fibronectin and laminin, on the surface of *E. coli* YMel in the biofilm, negative staining was performed. Figure 4 shows a fine structure composed of thin fibers that suggest curli expression in YMel, but such a structure was not found in the curli-deficient mutant YMel-1.

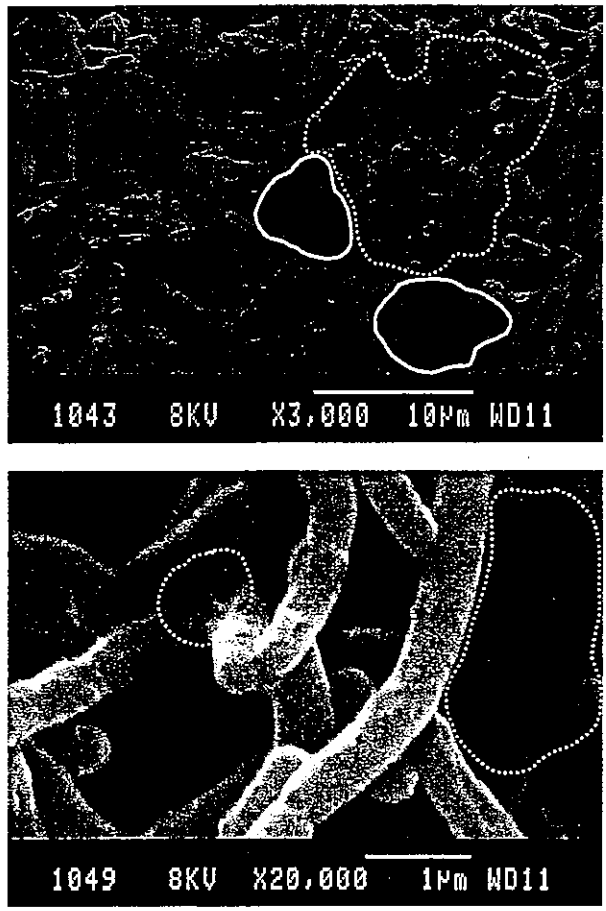

Figure 3. SEM photographs of biofilm on a glass slide at 24 h of incubation. Solid and broken lines indicate water channel regions and the dense parts of the biofilm, respectively.

Quantitative analysis

To quantify YMel cells that adhered to the PU film, round PU sheets that were incubated with YMel cells for up to 24 h postplating under static condition were subjected to gentle washing with PBS to remove nonadhering YMel cells, and then sonicated in PBS to detach all the adhered YMel cells. The fluorescence intensity of PBS containing detached YMel cells was measured with a fluorometer. In principle, the fluorescence intensity derived from GFP should correlate with the number of detached viable YMel cells by the plate count method. In fact, as shown in Figure 5, the fluorescence intensity highly correlated with the number of viable cells (correlation factor: 0.9997). The effect of the initial concentrations of YMel cells (2×10^3, 2×10^4, and 2×10^5 CFU/mL) on proliferation was studied (Fig. 6). The fluorescence intensity of PBS containing detached YMel cells increased as the initial cell concentration increased for up to 12 h of incubation. The higher the initial cell concentration, the higher the growth rate. However, after 12-h incubation, the flu-

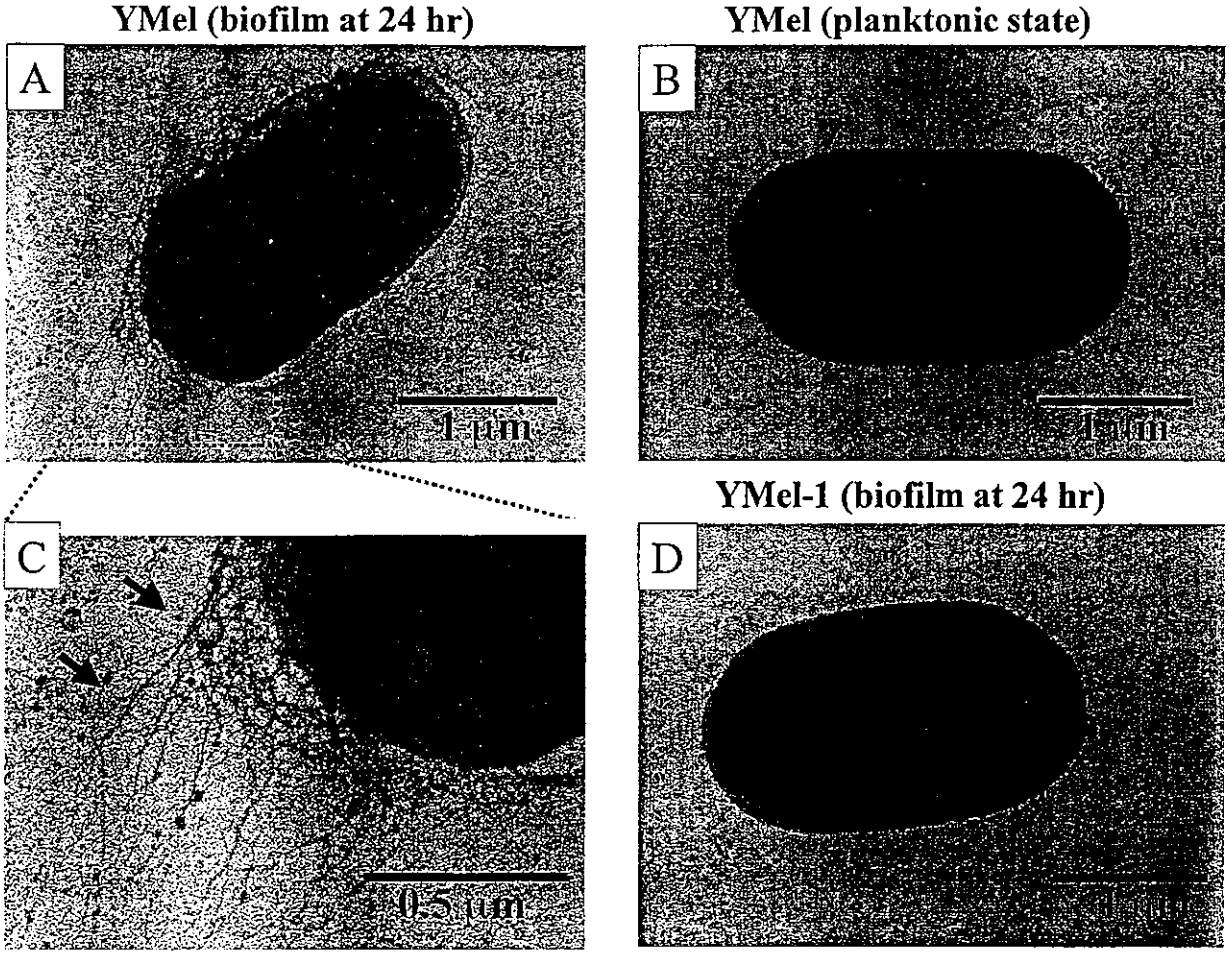

Figure 4. Transmission electron microscopic photographs by negative staining. (A) YMel in biofilm at 24 h; (B) YMel in planktonic state; (C) YMel in biofilm at 24 h with high magnification; and (D) YMel-1 in biofilm at 24 h. Arrows demonstrate curli.

orescence intensity remained almost constant, irrespective of the initial cell concentration.

Precoated-protein-dependent bacterial adhesion

To evaluate the effect of precoated proteins on bacterial adhesion, YMel was examined on round PU sheets precoated with the following proteins: fibronectin, vitronectin, and albumin (note that fibronectin and vitronectin are cell-adhesive, and albumin is non-cell-adhesive). As shown in Figure 7, for up to 12 h of incubation, there was a small significant difference in the number of adherent cells, irrespective of the type of precoated protein. However, at 24 h of incubation, the difference in the number of adherent cells was noted. The highest cell proliferation was observed on the fibronectin-coated surface, followed by the vitronectin-coated one, the proliferation potential of which was slightly higher than the noncoated surface; how-

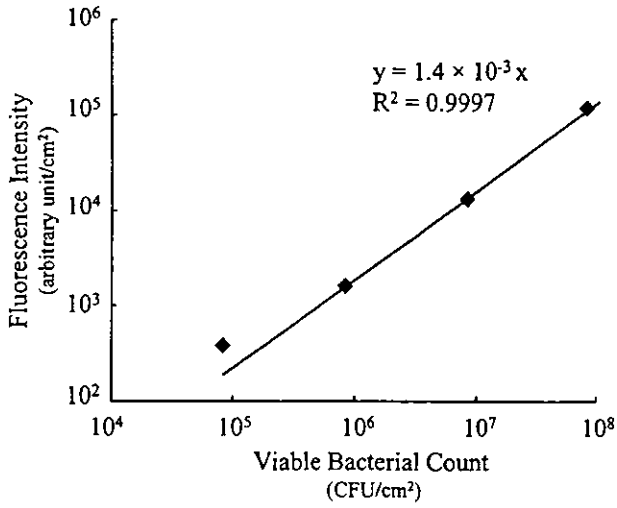

Figure 5. Correlation between fluorescence intensity and viable bacterial count in bacterial adhesion study at 24 h of incubation. The solution containing *E. coli* detached from PU sheets was diluted to different concentrations. Values are expressed as means ± SD.

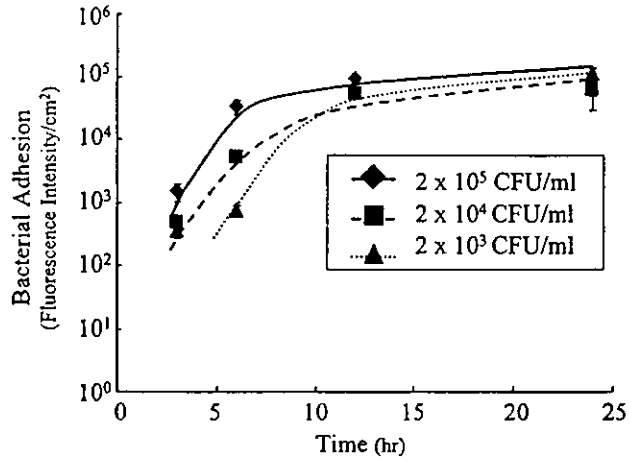

Figure 6. Time-dependent adhesion and proliferation of *E. coli* on PU. Initial concentration of bacterial cells: 2×10^3 (▲), 2×10^4 (■), 2×10^5, (◆) CFU/mL (n = 5). Values are expressed as means ± SD.

ever, there is only a small statistical difference between them. For the albumin-coated surface, although its initial adhesion potential is almost the same as that of the adhesive-protein-coated surfaces, minimal proliferation occured even with prolonged incubation time.

The curli-deficient mutant strain YMel-1 was used to determine the role of curli in bacterial adhesion. The curli-producing strain, YMel, and the curli-deficient isogenic mutant strain, YMel-1, were examined on PU surfaces with or without fibronectin coating. The number of adherent cells, measured by the plate count method, shows that the adhesion of YMel-1 was less than that of YMel to both fibronectin-coated and noncoated substrates. Precoating the PU sheets with fibronectin did not increase the adhesion of YMel-1 (Fig. 8), indicating that curli participate in fibronectin-mediated bacterial adhesion.

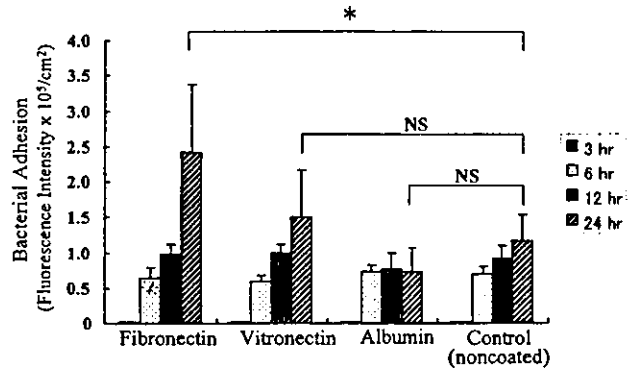

Figure 7. Bacterial adhesion to and proliferation on PU precoated with proteins at 3, 6, 12, and 24 h of incubations (n = 5). Control is noncoated PU. Values are expressed as means ± SD.

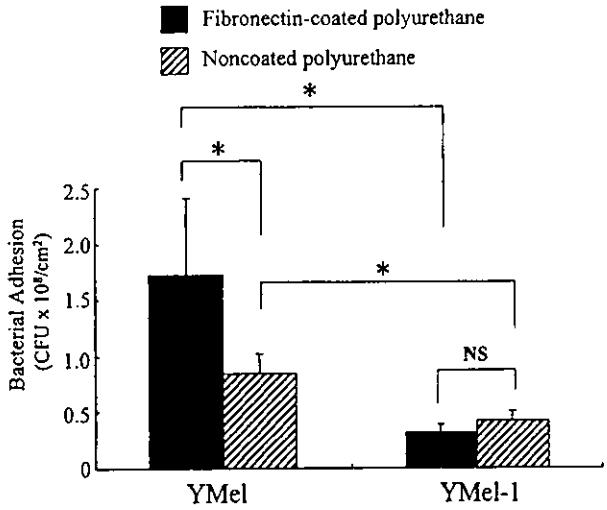

Figure 8. Bacterial adhesion and proliferation of curli-producing strain, YMel, and curli-deficient isogenic mutant strain, YMel-1 in fibronectin-coated PU and noncoated PU at 24 h of incubation (n = 5). Adhesion was determined by the plate count method. Values are expressed as means ± SD.

DISCUSSION

Bacterial adhesion is an important initial step in infection at the site of implanted biomaterials, which often causes life-threatening events in clinical situations.[1,2] Among bacteria capable of foreign-body-induced infection, *E. coli* is an important pathogen in the blockade of biliary stents or urinary catheters. The understanding of biofilm formation on synthetic biomaterials and the quantitative detection method for biofilm are key issues leading to the surface design of biomaterials with a high antibacterial adhesion potential. Electron microscopy has been used to examine biofilms on various materials.[9] However, sample preparation for electron microscopic observation requires sample dehydration, during which biofilms are often easily collapsed, structurally damaged, or destroyed. These dehydrated samples provide a deceivingly simplistic view of biofilms.[10]

To overcome this problem, we utilized fluorescent-compound-labeled *E. coli* strains that were transformed with a plasmid harboring the gene encoding GFP from jellyfish *Aequorea victoria* as an *in situ* cell marker. EPS are mainly responsible for the morphology and function of biofilms, and are considered to be key components that determine the physicochemical and biological properties of biofilms.[10,18] The co-use of GFP for bacteria and a fluorescent-compound-labeled marker specific to EPS in CLSM study provides new insights into the structure and nature of biofilm formation.

In our study, the imaging of 3D fine structures was acquired using fully hydrated samples for CLSM without any complex fixation such as the dehydration

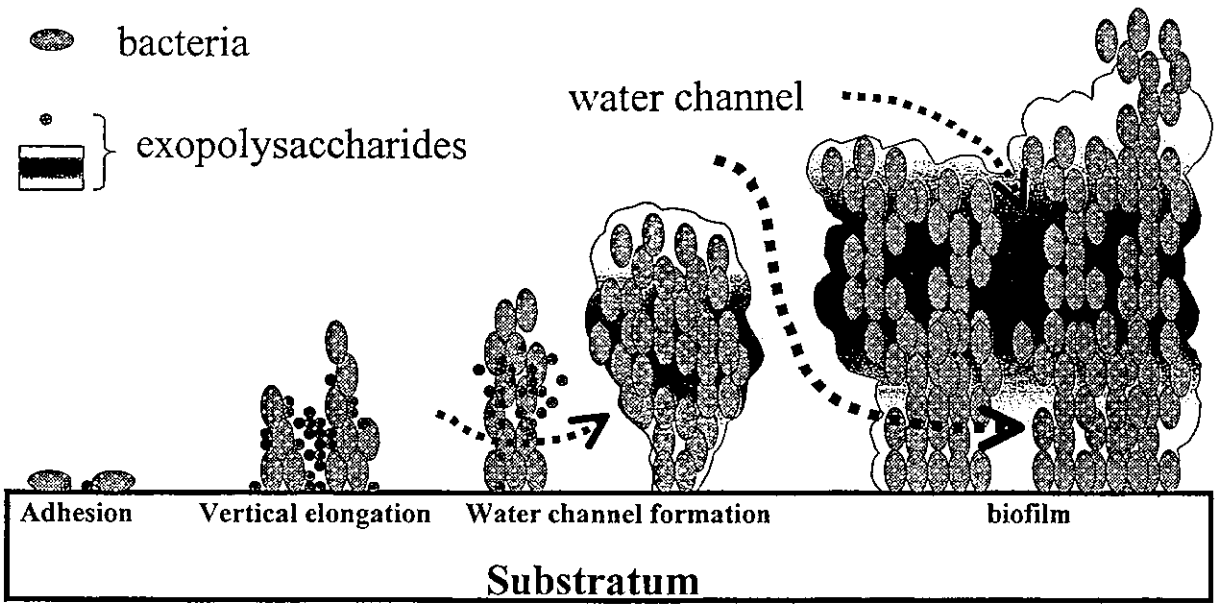

Figure 9. Scheme of time-dependent formation of biofilm architecture.

necessary in electron microscopy. In the early phase [3 h after plating: Figs. 1 and 2(A)], *E. coli* YMel emitting green fluorescence spottily aggregated on the PU surface and then vertically elongated. The number of aggregates increased with incubation time and scattered EPS-rich domains were observed [Figs. 1 and 2(A)]. Finally, a 3D structure including water channels was formed. The thickness of the biofilm increased with time, reaching to several tens of microns at 24 h after plating [Fig. 2(B)]. The channels as integral parts of the biofilm structure, which were identified as a black spotty area at 12 and 24 h of incubations (Fig. 1), are, in essence, the lifeline of the system, because they provide a means of circulating nutrients as well as exchanging metabolic products such as oxygen.[10] Interestingly, a dense interpenetrable structure of biofilm composed of *E. coli* and EPS, which was observed as the yellow region in Figures 1 and 2, existed at the middle part of the thick biofilm. Such time-dependent morphological events including bacterial adhesion, the secretion and organization of EPS, colony formation, and biofilm formation with water channels are shown in Figure 9.

As for the quantification of *E. coli* cells in biofilms, the fluorescence intensity of GFP expressed by adhered *E. coli* cells, which is directly proportional to the viable-bacterial count obtained by the plate count method (Fig. 5), allows us to easily and rapidly determine the number of adhered *E. coli* cells as compared with the conventional plate count method which requires overnight culture to detect colony formation. The growth rate of the *E. coli* cells examined for up to 24 h showed that the number of adhered and proliferated *E. coli* cells increased exponentially with time up to 12 h, and then appeared to increase at a markedly reduced rate with prolonged time, regardless of the initial bacterial cell concentration.

Many studies have reported that bacterial adhesion to and biofilm formation on material surfaces are affected by the type of protein adsorbed to the surfaces.[19-22] In the present study, three kinds of protein were preadsorbed: fibronectin and vitronectin as cell-adhesive proteins, and albumin as a non-cell-adhesive protein. Regardless of the presence or absence and the type of preadsorbed protein, there was only a small difference in the number of bacterial adhesion up to 12 h. Among the proteins tested, only fibronectin exhibited a markedly high proliferation activity only at 24 h of incubation, whereas albumin exhibited a high inhibitory activity against bacterial proliferation at 24 h of incubation. There is a small difference in bacterial proliferation activity between the vitronectin-coated and noncoated PU surfaces. This may be because the *E. coli* YMel does not produce curli in the early phase for up to 12 h of incubation but produces abundant curli (Fig. 4) in the biofilm at 24 h of incubation, although YMel does not produce curli in the planktonic state at 37°C.[23] These results are consistent with the finding by Kikuchi et al:[24] that curli were expressed in biofilm after growth at 37°C. Because curli specifically bind to fibronectin and are associated with biofilm maturation, curli-mediated biofilm formation occurred on the fibronectin-coated PU surface with a prolonged incubation time. However, the curli-deficient isogenic mutant, YMel-1, did not enhance bacterial adhesion and proliferation on the fibronectin-coated PU surface (Fig. 8).

In conclusion, we developed a novel method of deter-

mining morphological events during biofilm formation on synthetic polymers using GFP-expressing *E. coli* under CLSM observation, without the destruction of very fragile 3D structures, which may help logical surface design with a high antibacterial potential.

The authors thank T. Kikuchi, K. Yasutake, E. Koga, and M. Sato for technical assistance, and T. Kanemaru and A. Takade for electron microscopic examination.

References

1. An YH, Friedman RJ. Concise review of mechanisms of bacterial adhesion to biomaterial surfaces. J Biomed Mater Res 1998;43:338–348.
2. Gristina AG. Biomaterial-centered infection: microbial adhesion versus tissue integration. Science 1987;237:1588–1595.
3. Davies D. Understanding biofilm resistance to antibacterial agents. Nat Rev Drug Discov 2003;2:114–122.
4. Sung JY, Leung JW, Shaffer EA, Lam K, Costerton JW. Bacterial biofilm, brown pigment stone and blockage of biliary stents. J Gastroenterol Hepatol 1993;8:28–34.
5. Bryers JD, Hendricks S. Bacterial infection of biomaterials. Ann NY Acad Sci 1997;31:127–137.
6. Higashi JM, Wang IW, Shlaes DM, Anderson JM, Marchant RE. Adhesion of *Staphylococcus epidermidis* and transposon mutant strains to hydrophobic polyethylene. J Biomed Mater Res 1998; 39:341–350.
7. Merritt K, Gaind A, Anderson JM. Detection of bacterial adherence on biomedical polymers. J Biomed Mater Res 1998;39: 415–422.
8. Speer AG, Cotton PB, Rode J, Seddon AM, Neal CR, Holton J, Costerton JW. Biliary stent blockage with bacterial biofilm. A light and electron microscopy study. Ann Intern Med 1988;108: 546–553.
9. van Berkel AM, van Marle J, van Veen H, Groen AK, Huibregtse K. A scanning electron microscopic study of biliary stent materials. Gastrointest Endosc 2000;51:19–22.
10. Davey ME, O'toole GA. Microbial biofilms: from ecology to molecular genetics. Microbiol Mol Biol Rev 2000;64:847–867.
11. Cowan SE, Gilbert E, Khlebnikov A, Keasling JD. Dual labeling with green fluorescent proteins for confocal microscopy. Appl Environ Microbiol 2000;66:413–418.
12. Decho AW, Kawaguchi T. Confocal imaging of *in situ* natural microbial communities and their extracellular polymeric secretions using Nanoplast resin. Biotechniques 1999; 27:1246–1252.
13. Strathmann M, Wingender J, Flemming HC. Application of fluorescently labelled lectins for the visualization and biochemical characterization of polysaccharides in biofilms of *Pseudomonas aeruginosa*. J Microbiol Methods 2002;50:237–248.
14. Olsen A, Wick MJ, Morgelin M, Bjorck L. Curli, fibrous surface proteins of *Escherichia coli*, interact with major histocompatibility complex class I molecules. Infect Immun 1998;66:944–949.
15. Prigent Combaret C, Prensier G, Le Thi TT, Vidal O, Lejeune P, Dorel C. Developmental pathway for biofilm formation in curli-producing *Escherichia coli* strains: role of flagella, curli and colanic acid. Environ Microbiol 2000;2:450–464.
16. Olsen A, Jonsson A, Normark S. Fibronectin binding mediated by a novel class of surface organelles on *Escherichia coli*. Nature 1989;338:652–655.
17. Andersen JB, Sternberg C, Poulsen LK, Bjorn SP, Givskov M, Molin S. New unstable variants of green fluorescent protein for studies of transient gene expression in bacteria. Appl Environ Microbiol 1998;64:2240–2246.
18. Danese PN, Pratt LA, Kolter R. Exopolysaccharide production is required for development of *Escherichia coli* K-12 biofilm architecture. J Bacteriol 2000;182:3593–3596.
19. Froman G, Switalski LM, Faris A, Wadstrom T, Hook M. Binding of *Escherichia coli* to fibronectin. A mechanism of tissue adherence. J Biol Chem 1984;259:14899–14905.
20. Yu JL, Ljungh A, Andersson R, Jakab E, Bengmark S, Wadstrom T. Promotion of *Escherichia coli* adherence to rubber slices by adsorbed fibronectin. J Med Microbiol 1994;41:133–138.
21. Yu JL, Andersson R, Wang LQ, Bengmark S, Ljungh A. Fibronectin on the surface of biliary drain materials: a role in bacterial adherence. J Surg Res 1995;59:596–600.
22. Yu JL, Andersson R, Ljungh A. Protein adsorption and bacterial adhesion to biliary stent materials. J Surg Res 1996;62:69–73.
23. Bian Z, Brauner A, Li Y, Normark S. Expression of and cytokine activation by *Escherichia coli* curli fibers in human sepsis. J Infect Dis 2000;181:602–612.
24. Kikuchi T, Mizunoe Y, Takade A, Yoshida S. Curli is required for development of biofilm architecture in *Escherichia coli* K-12 and enhance bacterial adherence to human uroepithelial cells. In preparation.

Photocurable Biodegradable Liquid Copolymers: Synthesis of Acrylate-End-Capped Trimethylene Carbonate-Based Prepolymers, Photocuring, and Hydrolysis

Takehisa Matsuda, Il Keun Kwon, and Satoru Kidoaki

Division of Biomedical Engineering, Graduate School of Medicine, Kyushu University, 3-1-1 Maidashi, Higashi-ku, Fukuoka 812-8582, Japan

BioMACROMOLECULES

Reprinted from
Volume 5, Number 2, Pages 295–305

Photocurable Biodegradable Liquid Copolymers: Synthesis of Acrylate-End-Capped Trimethylene Carbonate-Based Prepolymers, Photocuring, and Hydrolysis

Takehisa Matsuda,* Il Keun Kwon, and Satoru Kidoaki

Division of Biomedical Engineering, Graduate School of Medicine, Kyushu University, 3-1-1 Maidashi, Higashi-ku, Fukuoka 812-8582, Japan

Received July 9, 2003; Revised Manuscript Received October 10, 2003

Various photocurable liquid biodegradable trimethylene carbonate (TMC)-based (co)oligomers were prepared by ring-opening (co)polymerization of TMC with or without L-lactide (LL) using low molecular weight poly(ethylene glycol) (PEG) (mol wt 200, 600, or 1000) or trimethylolpropane (TMP) as an initiator. Resultant (co)oligomers were pastes, viscous liquids, or liquids at room temperature, depending on the monomer composition and monomer/initiator ratio. Liquid (co)oligomers were subsequently end-capped with acrylate groups. Upon visible-light irradiation in the presence of camphorquinone as a radical generator, rapid liquid-to-solid transformation occurred to produce photocured solid. The photocuring yield increased with photoirradiation time, photointensity, and camphorquinone concentration. The photocured polymers derived from low molecular weight PEG (PEG200) and TMP exhibited much reduced hydrolysis potential compared with PEG1000-derived polymers in terms of weight loss, water uptake, and swelling depth. Force−distance curve measurements by nanoindentation using atomic force microscopy clearly showed that Young's moduli of the photocured polymer films decreased with increasing hydrolysis time. Their potential biomedical applications are discussed.

Introduction

Biodegradable polymers such as high molecular weight polyesters have been widely used in biomedical applications including structural supports such as sutures or bone pins, matrixes for controlled release of drugs, and scaffolds for tissue-engineered devices.[1−6] On the other hand, less attention has been paid to liquid photocurable low molecular weight (co)oligomers or prepolymers. If a biodegradable liquid prepolymer can be rapidly transformed into a solid by photoirradiation with visible or ultraviolet light in the presence of an appropriate photoinduced radical generator, such versatility may provide additional benefits in medical applications. The advantages of photopolymerization over other chemical or physical cross-linking techniques are (1) rapid curing that proceeds at room temperature and (2) in situ spatial and temporal control of the polymerization. These allow development of injectable gelable mold and in situ gelable drug-releasing matrix,[7,8] and precision fabrication including macroshaping of a device, surface microarchitecturing, and scaffold design for engineered tissues and artificial implants.[9,10]

The preparation of biodegradable liquid polymers is limited within a certain range of compositions and molar ratios of (co)polyesters. Conventional polyesters such as poly(glycolic acid) (PGA), poly(L-lactic acid) (PLLA), and poly(ϵ-caprolactone) (PCL) are crystallizable solids with a high glass transition temperatures (T_g). On the other hand, aliphatic poly(carbonate)s have relatively low T_g and are amorphous in nature. Poly(trimethylene carbonate) (PTMC), which has a low T_g (−38 to −17 °C) that depends on the molecular weight, is amorphous and exhibits an extremely slow degradation rate in water compared with polyesters.[11−13] The oligomer of TMC and its co-oligomer with CL are liquids.[14−19] Our previous studies showed that such co-oligomers end-capped with photoreactive groups such as coumarin,[14−17] phenyl azide,[18] or acrylate[19] were rapidly converted to solids upon photoirradiation. Their photocuring characteristics and hydrolytic behavior were studied in detail. In addition, stereolithographic microarchitectures were demonstrated using a custom-designed automated mobile photoirradiation apparatus.[9]

In this paper, as part of a series of our studies on biodegradable liquid photocurable prepolymers, we prepared liquid photocurable oligomers of TMC and co-oligomers with LL using low molecular weight poly(ethylene glycol) (PEG) or trimethylolpropane (TMP) as an initiator, followed by acrylation at terminal ends. Acrylate-end-capped liquid prepolymers were subjected to photocuring by visible-light irradiation. The dependence of photocuring characteristics on material properties and irradiation conditions was first described, followed by detailed analysis of hydrolytic behavior including surface erosion characteristics using confocal laser scanning microscopy (CLSM) to determine the depth profile of the water-swellable layer and using atomic force microscopy (AFM) to determine the mechanical

* To whom correspondence should be addressed. E-mail: matsuda@med.kyushu-u.ac.jp. Tel: +81-92-642-6210. Fax: +81-92-642-6212.

10.1021/bm034231k CCC: $27.50
Published on Web 12/12/2003

properties of the nanoscale water-swellable layer. Potential biomedical applications are discussed.

Experimental Section

General Procedure. All solvents and reagents were purchased from either Wako Pure Chemical Industries, Ltd. (Osaka, Japan) or Sigma-Aldrich Japan, Inc. (Tokyo, Japan). Trimethylene carbonate (TMC) was prepared according to the method described in our previous paper and recrystallized from a mixed solvent of ethyl acetate and hexane.[15] Trimethylolpropane (TMP) and L-lactide (LL) were recrystallized from acetone and ethyl acetate, respectively. Poly(ethylene glycol) (PEG) was purified by precipitation from cold hexane and subsequently dried under vacuum prior to use. Acryloyl chloride and camphorquinone were used as received without further purification. Other solvents and reagents were purified by distillation. ^{1}H NMR spectra were recorded on a JNM-AL300 (JEOL, Tokyo, Japan). Chemical shifts are given in δ values from Me_4Si as an internal standard. The number-average molecular weight (M_n) of each polymer was determined by gel permeation chromatography (GPC), which was carried out on a high-performance liquid chromatograph (HPLC, JASCO-JMBS, Tokyo, Japan) equipped with a TSK-GEL column α-3000 (TOSOH, Tokyo, Japan) using PEG as a standard and tetrahydrofuran (THF) as a solvent. Visible-light irradiation was carried out using a TOKUSO Power Lite (xenon lamp with UV and IR cutoff filter, Tokyo, Japan), and irradiation intensity was measured with a photometer (Laser power meter HP-1: Pneum Co., Ltd., Saitama, Japan) at 488 nm.

Synthesis of (Co)Oligomer. A typical procedure for the preparation was as follows. A reaction mixture of 0.33 M tin(II) 2-ethylhexanoate solution in toluene (35 μL, 12 μmol) as a catalyst, PEG (mol wt 1000, 7.6 g, 7.6 mmol), and TMC (10.21 g, 100 mmol) was stirred for 4 h at 200 °C, followed by heating for 2 h at 160 °C in a 100 mL round-bottom flask under a N_2 atmosphere. Then the solution was cooled, dissolved in dichloromethane, and added dropwise into an excess of hexane. Upon decantation of the hexane, the precipitated viscous liquid was redissolved in dichloromethane and again precipitated from excess hexane. After hexane was removed by vacuum-drying at 50 °C for 1 day, a viscous liquid at room temperature was obtained. Analysis of this liquid showed the following results: yield = 16.9 g (95%); $M_n = 2.24 \times 10^3$ (eluent, THF); ^{1}H NMR (300 MHz, $CDCl_3$, ppm) $\delta = 2.06$ (multiplet), 3.65 (triplet), and 4.24 (multiplet).

Synthesis of Acrylate-End-Capped Prepolymer. A representative procedure for acrylation of terminal ends of the oligomers is as follows. The prepolymer (16.5 g) was dissolved in 100 mL of dichloromethane in a 200 mL round-bottom flask cooled to 0 °C. Acryloyl chloride (6 mL) was added to this flask under N_2 atmosphere and the reaction mixture was stirred for 8 h at 50 °C. The prepolymer was precipitated from excess hexane and dried at 30 °C under vacuum for 1 day. The yield was 16.8 g (94%). The acrylate content was determined from the relative peak intensities in the ^{1}H NMR spectra between the vinyl group and PEG or TMP unit yielding the following results: ^{1}H NMR (300 MHz, $CDCl_3$, ppm) $\delta = 2.05$ (multiplet), 3.65 (doublet), 4.24 (multiplet), 5.85 (doublet), 6.12 (quartet), and 6.42 (doublet).

Visible-Light-Induced Photocuring. Camphorquinone-containing dichoromethane solution (20 wt %) was added to viscous liquid acrylated oligomer and stirred thoroughly with a high speed rotating shaker and subsequently was subjected to solvent evaporation and degassing under reduced pressure. This is added into the Experimental Section. Round-shaped liquid films (ϕ = 10 mm) of comphorquinone-containing acrylated oligomers were irradiated with visible light. After immersion in dichloromethane to remove the soluble fraction, the insoluble polymer was dried and weighed. The photocuring yield was defined as the weight percentage of the insoluble part (W_g) against that of the initial prepolymer (W): $W_g/W \times 100$.

Water Contact Angle. The surface wettability of the photocured films was evaluated by measuring the static contact angles (advancing and receding) toward deionized water using the sessile drop method with a contact angle meter (CA-D, Kyowa Interface Co. Ltd., Tokyo, Japan) at 25 °C.

Hydrolytic Degradation. Photocured films (10 mm × 10 mm × 1 mm) were weighed (initial weight; W_O) and immersed in 0.01 M aqueous phosphate-buffered solution (PBS, pH 7.4) at 37 °C for up to 4 weeks under static conditions. After each 1-week period, the swollen weight (W_S) and dried weight (W_D) of the films were measured after wiping the surface with paper and after vacuum-drying, respectively. The weight loss (WL) and water adsorptivity (WA) upon hydrolysis on a weekly basis were evaluated as

$$\mathrm{WL}\,(\%) = 100([W_O - W_D]/W_O) \quad \text{and}$$

$$\mathrm{WA}\,(\%) = 100([W_S - W_D]/W_D)$$

Surface Topological Observation. The hydrolytic behavior of the photocured film surface was observed by scanning electron microscopy (SEM, JSM-840A, JEOL Ltd., Tokyo, Japan) after sputter-coating with gold and by atomic force microscopy (AFM, NBV100, Olympus Optical Co., Ltd., Tokyo, Japan; AFM controller & software, Nanoscope IIIa, Digital Instrument, NY). In AFM, the image was obtained by contact-mode scanning in PBS. A silicon−nitride soft cantilever with a spring constant of 0.027 N/m (Biolever, Olympus) was used to minimize the scanning-load-dependent geometric change, and the applied load was set to 0.8 nN.

Swelling Depth. Swelling depth was determined by a confocal laser scanning microscope (CLSM, Radiance 2000, Bio-Rad laboratories Inc., Hercules, CA). Each nonhydrolyzed and 4-week-hydrolyzed sample (5 mm × 5 mm × 1 mm) was immersed in aqueous rose bengal solution (10 mg/mL) for 2 days at 25 °C. The central part of the swollen specimen was sliced for visual observation of the cross section. The fluorescence intensity of the cross-sectional image was determined by NIH Image Software (version 1.58).

Microscopic Indentation Test. Two hundred microliters of prepolymer was coated on a glass dish (Iwaki Glass,

Scheme 1. Schematics of Preparation Routes of (Co)Oligomer and Acrylate-End-Capped Prepolymer and Photocuring.

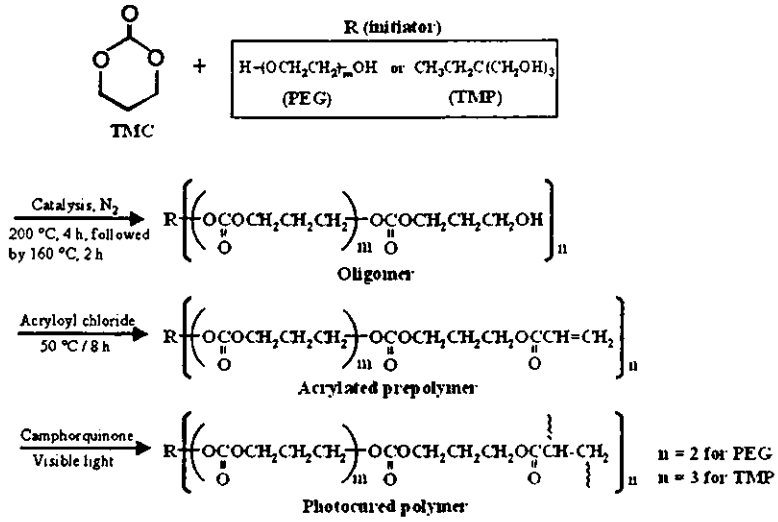

Japan; diameter of well = 15 cm, thickness of the well = ca. 1 mm), photocured, and then immersed in PBS. The AFM force−distance curves ($f-d$ curves) of photocured samples were measured in the glass dish using a cantilever with a spring constant of 0.68 N/m at seven randomly chosen locations on each sample in PBS. The $f-d$ curves were sequentially measured more than three times and typical curves were recorded by computer software after confirming the minimum fluctuations. The frequency of the tip approach/retract cycle was chosen to be 1.5 Hz to minimize the noise fluctuation in a single $f-d$ curve. Raw $f-d$ curves were converted to force-versus-indentation curves ($F-\delta$ curves).[20] Young's moduli of the surface of each sample were evaluated from the $F-\delta$ curves by fitting to a Hertz model.[20,21] Two kinds of model for fitting were employed, depending on the profile of the $F-\delta$ curve: a Hertz model for a conical tip (type A and B fittings) or for a flat-ended cylindrical tip (type C fitting) as described below (see Scheme 2).

Type A and B Fittings. For a conical tip with a semivertical angle α, the total force F as a function of the indentation δ is given as[20]

$$F_{\text{cone}}(\delta) = \frac{2\tan\alpha}{\pi}\frac{E}{1-\mu^2}\delta^2 \qquad (1)$$

where E is Young's modulus and μ is the Poisson ratio. The terms α and μ were 30° and 0.5, respectively.

Type C Fitting. A flat-ended cylindrical tip with radius R gives a linear $F-\delta$ relationship as[20]

$$F_{\text{cylinder}}(\delta) = 2RE\delta \qquad (2)$$

where R was 20 nm based on the radius of curvature of the tip (manufacturer's data).

Type A and B fitting analyses were performed on the $F-\delta^2$ plot, while the type C fitting was used for the case in which the $F-\delta$ plot showed an almost linear profile. If the sample shows ideal homogeneous elasticity, the $F-\delta^2$ plot would fit the linear profile in the case of a conical tip (type A fitting, see Scheme 2a). However, many samples typically exhibit nonlinear $F-\delta^2$ plots with positive or negative curvatures. For the positive curvature, which is interpreted as the coupling of two lines with different slopes, the two-step fitting was adopted (type B fitting, see Scheme 2b). In the first step, a line fitting was applied to the initially indented region and the Young's modulus of the outermost surface region, E_1, was calculated from the slope. In the second step, a line fitting was performed for the fully indented region and Young's modulus of the subsurface, E_2, was calculated from the slope. The thickness of the highly swollen outermost surface (T) was evaluated from the intersection between the two-step fitting lines. On the other hand, for the negative curvature, linear fitting of an almost linear $F-\delta$ plot was adopted (type C fitting, see Scheme 2c). From the one-step fitting (type A and C fitting), Young's modulus (E) could be evaluated.

Statistical Analysis. All of the quantitative results were expressed as a mean ± SD. Statistical analysis was carried out using an ANOVA with a Scheffé test post hoc, $p < 0.05$. All statistical analyses were performed using Statview for Windows (SAS Institute, Inc., Copyright 1992−1998), version 5.0.

Results

Preparation of Liquid Acrylate-End-Capped TMC-Based Prepolymers. Scheme 1 illustrates the sequential reaction steps for preparation of a (co)oligomer, acrylation of (co)oligomer at both terminal ends, and photocuring. A series of TMC-based (co)oligomers was synthesized by ring-opening (co)polymerization in the presence of low molecular weight PEG (mol wt 200, 600, or 1000) or TMP as an initiator in the presence of stannic octanate as a catalyst. The PEG-initiated oligomer is linear, and the TMP-initiated oligomer has a three-armed branch. Table 1 summarizes the reaction conditions, monomer compositions, molecular weights, and the physical states of the (co)oligomers prepared. The compositions of (co)oligomers were determined by ^{1}H NMR spectroscopy (Figure 1a). The number-average molecular weights of the (co)oligomers, determined or estimated by GPC, ranged from approximately 650 to 3400. An increase in the ratio of monomer to initiator resulted in an increase in the number-average molecular weight of (co)oligomers,

Table 1. TMC-Based Biodegradable (Co)Oligomers[a]

monomer			monomer feed ratio		prepolymer composition[b]	molecular weight		physical state
M1	M2	initiator (I)	M1/M2/I	yield (%)	M1/M2/I	M_n	M_w/M_n	at 25 °C
TMC		PEG 1000	1:0:0.028	92.6	1:0:0.029	3380	2.01	viscous liquid
		PEG 1000	1:0:0.076	94.7	1:0:0.075	2240	1.84	liquid
		PEG 1000	1:0:0.100	94.5	1:0:0.107	1810	1.43	paste
		PEG 1000	1:0:0.250	92.5	1:0:0.268	1140	1.26	paste
		PEG 600	1:0:0.076	93.8	1:0:0.077	2180	1.59	liquid
		PEG 600	1:0:0.250	93.6	1:0:0.263	1040	1.48	liquid
		PEG 200	1:0:0.076	95.1	1:0:0.074	1630	1.52	viscous liquid
		PEG 200	1:0:0.250	93.4	1:0:0.247	650	1.36	liquid
		TMP	1:0:0.050	90.2	1:0:0.050	1690	1.68	viscous liquid
		TMP	1:0:0.167	94.4	1:0:0.168	920	1.42	liquid
TMC	L-lactide (LL)	PEG 1000	0.5:0.5:0.76	89.8	0.51:0.49:0.078	2410	1.27	liquid
		PEG 1000	0.5:0.5:0.250	84.4	0.63:0.37:0.313	1390	1.22	paste
		PEG 600	0.5:0.5:0.76	90.6	0.52:0.48:0.081	2370	1.49	viscous liquid
		PEG 200	0.5:0.5:0.76	88.7	0.52:0.48:0.086	2290	1.48	viscous liquid

[a] Reaction conditions were 200 °C for 4 h, followed by 160 °C for 2 h. [b] Determined by ^{1}H-NMR. [c] Determined by GPC in THF (PEG standard. M_n is number-average molecular weight; M_w is weight-average molecular weight; M_w/M_n is polydispersity. The molecular weight of the three-armed TMP-based oligomers estimated from the PEG standard, which is theoretically only applicable to linear polymers, may be overestimated because the hydrodynamic radius of a three-armed polymer is not the same as the linear polymer at the equivalent molecular weight basis.

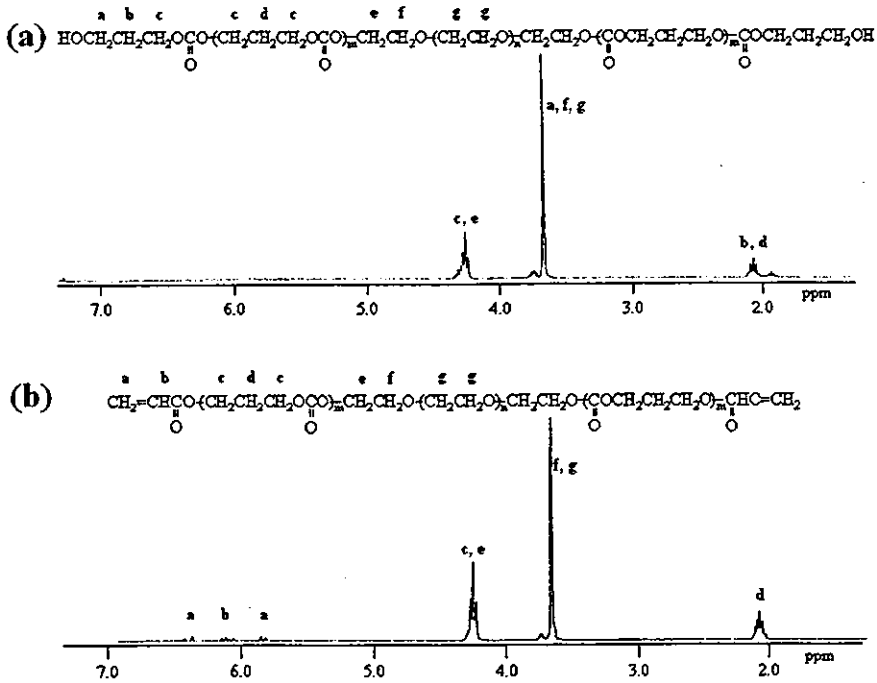

Figure 1. ^{1}H NMR spectrum and assignment of (a) (co)oligomer of PEG (molecular weight 1000) and TMC and (b) acrylate-end-capped prepolymer (**T/P1k**).

irrespective of the type of initiator. The yields of (co)-oligomers were approximately 85−95 wt %. The (co)-oligomer compositions were almost identical to those of the initial feeds. The resultant (co)oligomers were pastes, viscous liquids, or liquids at room temperature, depending on the monomer composition and the molar ratio of monomer to initiator. Among these (co)oligomers, several liquid (co)-oligomers were subjected to further acrylate end-capping by esterification using excess acryloyl chloride against the hydroxyl groups of the terminal ends of (co)oligomers. As shown in Table 2, 90−98% esterification was achieved, which was determined by ^{1}H NMR spectroscopy (Figure 1b). All of the acrylate-end-capped prepolymers thus prepared were liquid [the code names of photocurable prepolymers such as **T/P1k**, **T/P200**, **T/TMP**, and **T/L/P1k** are in Table 2. T and L denote TMC and LL, respectively. P1k and P200 denote PEG with mol wt of 1000 and 200, respectively].

Photocuring Characteristics. Photopolymerization was carried out by visible light (xenon lamp with UV and IR cutoff filters) as a light source in the presence of camphorquinone as an initiator. The photocured polymers, which were not soluble in any organic solvent, were obtained, irrespective of the type of prepolymers. The dependence of photocuring characteristics on light intensity, camphorquinone concentration, liquid film thickness, and composition of prepolymer was systematically determined (Figure 2).

The effect of visible-light intensity on the irradiation time-dependent photocuring yield of **T/P1k** (Table 2) at a fixed

Table 2. Acrylate-End-Capped Liquid Biodegradable Prepolymers and the Surface Wettabilities of Photocured Films

		acrylate-end-capped prepolymer[a]		photocured films[b]		
prepolymer code	initiator	TMC/lactide/intiator	degree of acrylation (%)	gel yield (%)	advancing contact angle[c] nonhydrolyzed/ 4 weeks hydrolyzed	receding contact angle[c] nonhydrolyzed/ 4 weeks hydrolyzed
T/P1k	PEG 1000	1:0:0.076	97	92.7	23.8 ± 1.62/24.1 ± 1.88	<5.0/<5.0
T/P200	PEG 200	1:0:0.250	90	97.9	41.5 ± 2.55/42.2 ± 0.94	27.0 ± 3.56/13.0 ± 1.69
T/TMP	TMP	1:0:0.167	92	97.8	59.2 ± 1.50/61.6 ± 1.25	47.4 ± 5.33/28.5 ± 1.90
T/L/P1k	PEG 1000	0.5:0.5:0.076	94	90.4	32.3 ± 4.47/74.4 ± 1.85	9.7 ± 1.74/11.7 ± 1.16

[a] Determined by ^{1}H-NMR. [b] Photocuring conditions were liquid film of acrylate-end-capped prepolymers of thickness 1 mm under photoirradiation at the intensity of 100 mW/cm^2 for 1 min at room temperature with a camphorquinone concentration of 0.5 wt % of prepolymer. [c] Advancing and receding water contact angle measured using deionized water by the sessile drop method.

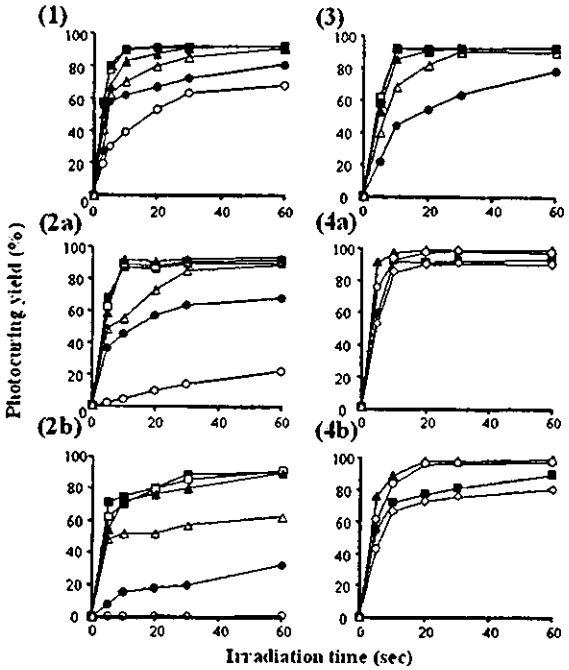

Figure 2. Dependence of photocuring yield of liquid acrylate-end-capped prepolymer films on photopolymerization conditions as a function of photoirradiation time: (1) effect of visible-light intensity on photocuring of **T/P1k** film (1 (○), 5 (●), 20 (△), 50 (▲), 100 (□), and 200 (■) mW/cm^2; camphorquinone concentration = 0.5 wt %; liquid film thickness = 1 mm); (2) effect of camphorquinone concentration on photocuring of **T/P1k** film (0 (○), 0.05 (●), 0.1 (△), 0.3 (▲), 0.5 (□), and 1 (■) wt %; light intensity = 100 mW/cm^2 (a) or 20 mW/cm^2 (b); liquid film thickness = 1 mm; (3) effect of liquid film thickness on photocuring of **T/P1k** film (1 (■), 3 (□), 5 (▲), 10 (△), and 20 (●) mm; light intensity = 100 mW/cm^2; camphorquinone concentration = 0.3 wt %); (4) effect of types of prepolymers on photocuring (**T/P1k** (■), **T/P200** (○), **T/TMP** (▲), and **T/L/P1k** (◇); light intensity = 100 mW/cm^2 (a) or 20 mW/cm^2 (b); camphorquinone concentration = 0.3 wt %; liquid film thickness = 1 mm.

concentration of camphorquinone (0.5 wt %) is shown in Figure 2-1. The yield increased with both irradiation time and light intensity. At higher light intensity (100 and 200 mW/cm^2), there was little difference in the photocuring kinetic characteristics, reaching a photocuring yield of approximately 90% within 10 s. The effect of camphorquinone concentration on the irradiation-time-dependent photocuring yield of **T/P1k** at the light intensities of 100 and 20 mW/cm^2 is shown in Figure 2-2a,2b, respectively. When camphorquinone concentration was increased, the yield increased with irradiation time. This tendency was more profound for high light intensity than low light intensity. For example, even in the absence of camphorquinone, photocuring yield increased with irradiation time at 100 mW/cm^2, whereas little photocured gel was produced at 20 mW/cm^2. At higher concentrations of camphorquinone, above 0.3 wt %, irrespective of light intensity, almost the same irradiation time dependence of photocuring yield was obtained. The effect of the liquid film thickness of the prepolymer **T/P1k** on irradiation-time dependence of photocuring yield was examined at liquid film thicknesses ranging from 1 to 20 mm. Below 10 mm thickness, over 90% of photocuring occurred within 30 s of photoirradiation as shown in Figure 2-3. The dependence of photocuring yield on irradiation time for different acrylate-end-capped prepolymers at high (100 mW/cm^2) and low (20 mW/cm^2) intensities is shown in Figure 2-4a,4b, respectively. The higher molecular weight prepolymers showed slightly lower photocuring characteristics, as shown in Figure 2-4a: yield of all of the prepolymers was above 90 wt % within 10 or 20 s at high-intensity irradiation (100 mW/cm^2).

Surface Wettability. The water contact angles (advancing and receding) of photocured polymer films before and after 4-week immersion in PBS are shown in Table 2. Before immersion into PBS, photocured polymers, P(**T/P1k**) and P(**T/L/P1k**), both of which were obtained using PEG1000 as an initiator, exhibited quite low advancing and receding angles, indicating that these photocured films were highly wettable. On the other hand, P(**T/P200**) film, obtained using PEG200, exhibited moderately low contact angles, whereas P(**T/TMP**) exhibited relatively high contact angles. Upon 4-week immersion in PBS, there were little differences in the advancing angles of photocured polymers except for P(**T/L/P1k**), which exhibited elevated advancing angles. Irrespective of type of photocured copolymers, quite low receding contact angles were noted.

Hydrolysis Characteristics. The hydrolytic characteristics of the photocured polymer films immersed in 0.01 M PBS at 37 °C were determined by several techniques: (I) weight loss and water uptake, (II) surface topological observations, (III) swelling depth, and (IV) changes of surface elastic properties.

Characterization of Hydrolytic Behavior (I): Weight Loss and Water Uptake. Figure 3 shows the dependence of weight loss (a) and water uptake (b) on time for films of four photocured polymers [P(**T/P1k**), P(**T/P200**), P(**T/TMP**), and P(**T/L/P1k**)]. Irrespective of the type of photocured polymer, the weight loss of the films gradually increased with immersion time. At 4 weeks of immersion, the films of P(**T/P200**) and P(**T/TMP**) showed weight losses of 4.3%

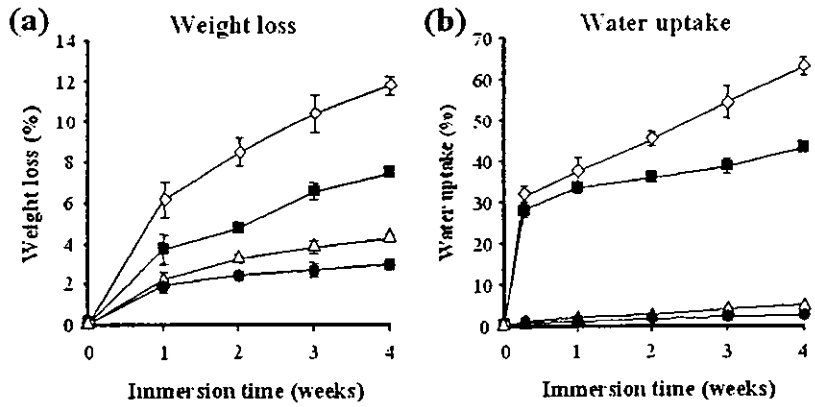

Figure 3. Weight loss (a) and water uptake (b) of photocured polymer films P(T/P1k (■), P(T/P200) (△), P(T/TMP) (●), and P(T/L/P1k) (◇) during degradation (n = 3).

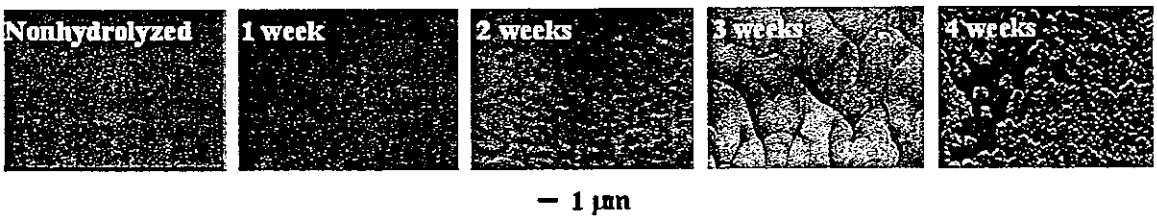

Figure 4. SEM images of photocured polymer, P(T/P1k), films for up to 4 weeks of immersion in PBS at 37 °C.

and 2.9%, respectively. PEG1000-based polymers, P(**T/P1k**)- and P(**T/L/P1k**), exhibited higher degradation rates than the former two photocured polymers: for example, weight loss after 4-week immersion of P(**T/L/P1k**) film was approximately 12%, which is almost four times larger than that of P(**T/TMP**). Initial two-day water uptakes of these PEG1000-based polymer films were about 30% and gradually increased with immersion time, while those of P(**T/P200**) and P(**T/TMP**) films were less than 5% even at 4 weeks of immersion.

Characterization of Hydrolytic Behavior (II): Surface Topological Observation. To characterize the topographical surface changes of the photocured polymer films subjected to hydrolysis, microscopic observations with SEM and AFM were performed. SEM images of P(**T/P1k**) films subjected to hydrolysis P(**T/P200**) for up to 4 weeks are shown in Figure 4. After being dried under vacuum for SEM observation, the films exhibited significant cracks on their surfaces after 3- and 4-week immersions, whereas much less hydrolyzable P(**T/P200**) film showed very smooth surfaces during the entire observation period (data are not shown), indicating that the dried P(**T/P1k**) film surface became roughened with immersion time. The AFM observation in PBS clearly showed the microtopological changes of the swollen surface of P(**T/P1k**) film during 6 weeks of hydrolysis as follows. Figure 5a,b shows height images of the film at different immersion periods and its cross-sectional analysis, respectively. At 5 h and 1 week of immersion, the film showed a slightly rough surface (roughness around 10 nm in height) probably due to irregular swelling of the surface with inhomogeneous morphological state. At 2 weeks of immersion, the surfaces became relatively smooth, suggesting that the swollen layer was flattened during this period. After 4 weeks of immersion, small indents or pits on the film surface probably caused by local erosion were observed, which were enlarged after further immersion (6 weeks). The depth of pits reached approximately 20 nm.

Characterization of Hydrolytic Behavior (III): Swelling Depth. The swelling depth profile of the photocured polymer films was determined by CLSM upon staining with aqueous rose bengal solution. For the photocured PEG1000-based polymers [P(**T/P1k**) and P(**T/L/P1k**)], the slices of films were uniformly and completely stained with the dye even before being subjected to hydrolysis, indicating that these films were already highly swollen prior to hydrolysis (Figure 6a). On the other hand, P(**T/P200**) and P(**T/TMP**) films exhibited a slight staining only on their outermost surface regions, both before and after hydrolysis. Figure 6b shows the depth profile of fluorescence intensity in the cross section of the films of P(**T/P200**) and P(**T/TMP**) before hydrolysis and after 4-week hydrolysis. In the nonhydrolyzed P(**T/P200**), although the fluorescence intensity and depth distribution, which reflect the degree of swelling, increased after 4 weeks of hydrolysis, swelling was limited to the outermost surface region but proceeded to deeper regions with immersion time. The least swellable photocured polymer, P(**T/TMP**), exhibited much less dye uptake and smaller depth of dye-stained section than those of P(**T/P200**). There was little difference in maximal fluorescent intensity and width between nonhydrolyzed and 4-week hydrolyzed P(**T/TMP**).

Characterization of Hydrolytic Behavior (IV): Surface Elastic Property. Micromechanical properties of the swollen surface region were determined using the microscopic indentation test by AFM in PBS. Figure 7 shows force–indentation curves ($F-\delta$ plots) of photocured polymers [P(**T/P1k**), P(**T/P200**), and P(**T/TMP**)], which were subjected to hydrolysis for up to 6 weeks in PBS. For the whole-body-swellable polymer, P(**T/P1k**), a marked time-dependent change in the $F-\delta$ curve was noticed. The indentation depth gradually increased with immersion time. Such a trend with

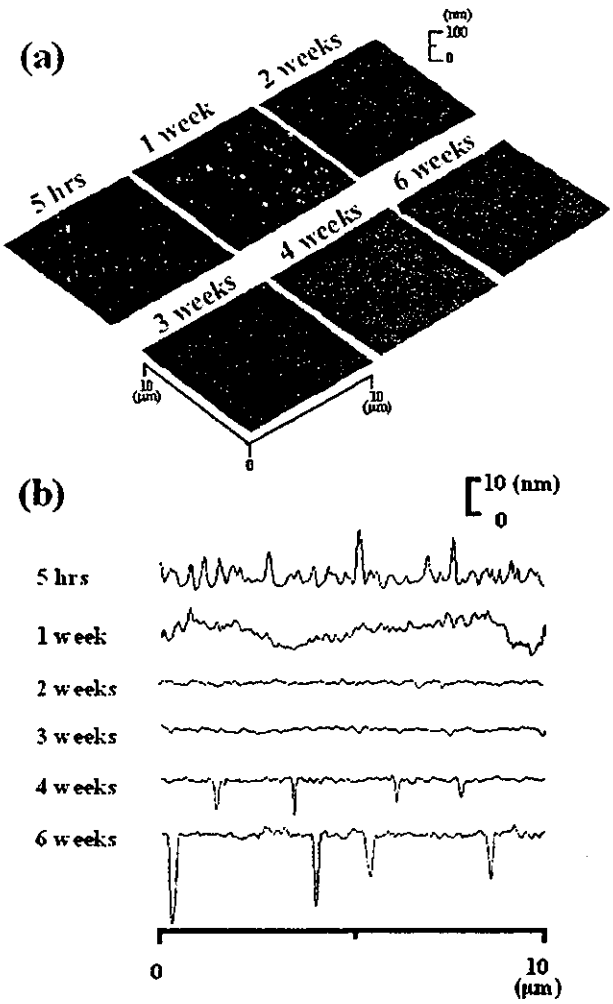

Figure 5. AFM (a) height images of photocured polymer (P(T/P1k)) films for up to 6 weeks of immersion in PBS at 37 °C and (b) section analysis of hydrolyzed polymer films.

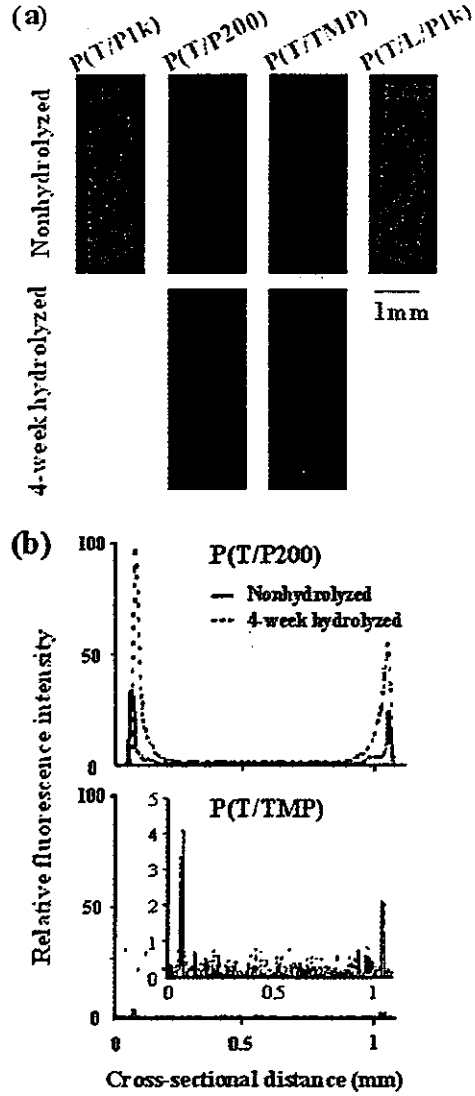

Figure 6. Distribution of fluorescence (a) at cross sections of nonhydrolyzed and 4-week hydrolyzed photocured polymer films stained with aqueous rose bengal solution and (b) fluorescence intensity distribution in cross sections of stained P(T/P200) and P(T/TMP)) films before (line) and after (dashed line) hydrolysis ($n = 5$).

less change was also observed for P(T/P200) the swelling of which was limited only to the surface region (Figure 6). In the case of the least swellable polymer, P(T/TMP), a minimal increase in indentation depth was observed during 6 weeks of immersion.

To quantify the elastic properties of the photocured polymers, fitting analyses employing Hertz models were performed according to the methods shown in Scheme 2. If the elastic property of the polymer obeys an "ideal" Hertz model for a conical tip, $F-\delta^2$ plots should have a linear profile (type A fitting in Figure 8b). However, many real $F-\delta^2$ plots exhibited significant curvatures: positive or negative except for those listed below, 4- and 6-week-immersed P(T/P1k) and 5-h- and 1-week-immersed P(T/P200) (Figure 8a). Positive curvature suggests that a higher index of δ is required to fit the original $F-\delta$ plot appropriately. However, index "2" for a conical-shaped tip is theoretically the highest one in the Hertz model. We interpreted such nonideal behavior of the $F-\delta^2$ plot as the coupling of the two linear parts, that is, two-step fitting (type B fitting in Figure 8b), which is caused by two heterogeneous layers at the surface region. On the other hand, the slightly negative curvature of the $F-\delta^2$ plot (plots of P(T/P1k) film after 5-h, 1-week, and 2-week hydrolyses, in which the slope of the initially indented region is steeper than that of the fully indented region) means that the original $F-\delta$ plot is more similar to a linear profile than to a quadratic profile. In this case, index "1" for the cylindrical tip Hertz model should be applied for fitting (type C fitting in Figure 8b).[20,21]

From the two-step fitting analysis for the $F-\delta^2$ plot with positive curvature (type B fitting), the slopes of the fitted lines for the initially indented region and for the fully indented region can be determined to give Young's moduli of the outermost surface region (E_1) and subsurface (E_2), respectively. In addition, from the intersection point between these two fitted lines, we deduced the characteristic thickness of the highly swollen outermost surface (T) taking into account that the significant change in elastic property was observed around the intersection point. Young's modulus (E) can only be evaluated for the surface of relatively thick mechanically uniform films from the fitting analysis of the $F-\delta^2$ plot with a linear equation (type A fitting) and the $F-\delta$ plot with a linear equation for the cylindrical tip (type C fitting).

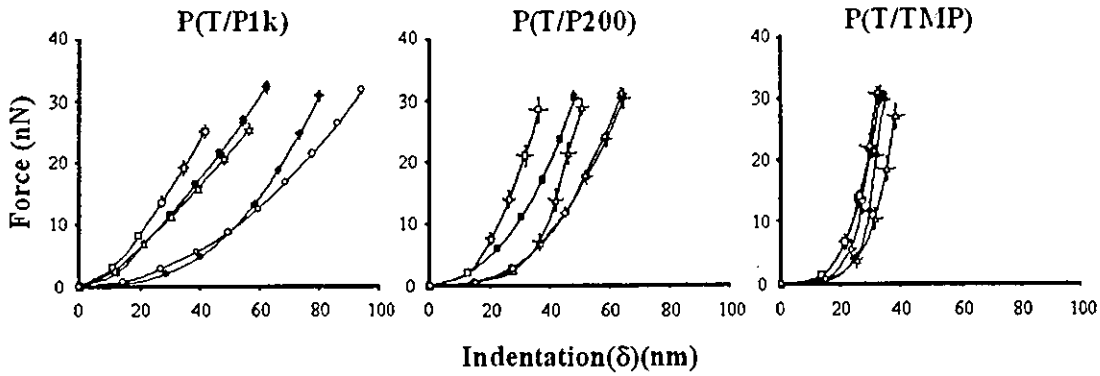

Figure 7. Force–indentation curves (F–δ curves) of photocured polymer (P(**T/P1k**), P(**T/P200**), and P(**T/TMP**)) films: 5 h (■), 1 week (□), 2 weeks (△), 4 weeks (●), and 6 weeks (○) of immersion in PBS (n = 7).

Scheme 2. Methods of Fitting Analyses of Nanoscopic Force–Indentation Curves by Hertz Models (1) for a Conical Tip with (a) Linear Fitting for F–δ^2 Plot (Type A Fitting) or (b) Two-Step Fitting for Biphasic F–δ^2 Plot (Type B Fitting) and (2) for a Flat-Ended Cylindrical Tip with (c) Linear Fitting for F–δ Plot (Type C Fitting)[a]

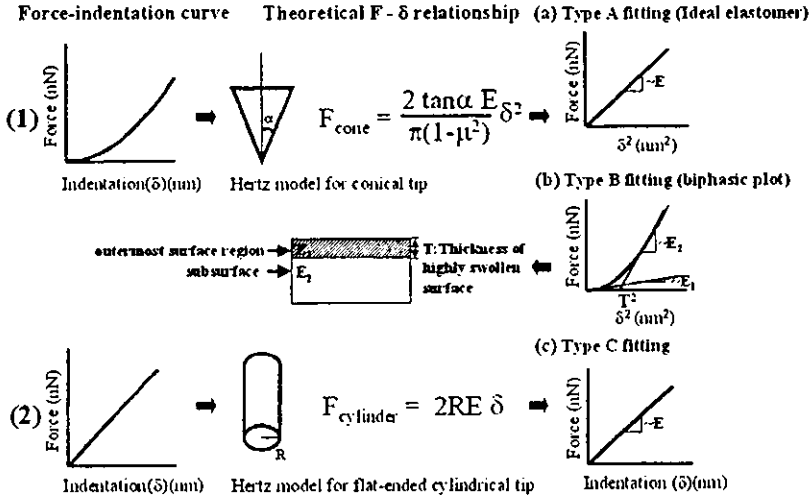

[a] The symbols are described in the Experimental Section.

Figure 9 shows hydrolysis time-dependent averaged E (calculated by the method described above) for the uniform surfaces and E_1 and E_2 for the mechanically biphasic-layered surfaces (n = 7). The most water-swellable polymer, P(**T/P1k**), exhibited a very low E ($E_1 = E_2$) of approximately 10 MPa, which tended to decrease with time (calculated using type C fitting for the early period and type A fitting for the later period). The less water-swellable polymer, P(**T/P200**), exhibited a linear F–δ^2 plot (type A fitting) at the very early stage of immersion but a biphasic plot (type B fitting) in the later period. A relatively large E was observed for an early period of hydrolysis; however, quite low E_1 (around 10 MPa, irrespective of immersion time) and reduced E_2 (around 40 MPa at 2 weeks and around 20 MPa at 4 and 6 weeks) were observed for a later period. Young's modulus tended to decrease with hydrolysis time. The least swellable polymer, P(**T/TMP**), exhibited a biphasic F–δ^2 plot: fairly large E_1 and large E_2. E_1 tended to decrease with time, whereas E_2 increased particularly at the later period of hydrolysis. Generally, E_2 was larger than E_1 for both P(**T/P200**) and P(**T/TMP**), indicating that the outermost surface region became softer than the bulk phase upon hydrolysis. As for the comparison of elasticities of different photocured polymer films at the surface region, Young's modulus increased in the following order: P(**T/P1k**) < P(**T/P200**) ≪ P(**T/TMP**) for any duration of hydrolysis.

Figure 10 shows the thickness (T) of the highly swollen outermost surface region for both P(**T/P200**) and P(**T/TMP**), which were determined from the intersection point in the type B fitting. The calculated thickness of P(**T/P200**) was approximately 40 nm at 2–6 weeks of immersion, while P(**T/TMP**) had a thickness of almost 25–28 nm during the entire course of hydrolysis up to 6 weeks.

Discussion

Liquid acrylated oligo(ester)- or oligo(carbonate)-based prepolymers with the ability to rapidly transform into a solid upon visible-light photoirradiation may find various medical applications such as drug delivery matrixes, photoconstructs of microarchitectural surfaces, micro- and macroshaped devices for implants and engineered tissues, and in situ formable molds. In our previous studies, liquid acrylated prepolymers composed of TMC and CL were prepared. The polymer composition, type of alcohol used as an initiator, its functionality-differentiated surface erosion rate, and the concomitant biodegradability of the photocured implants were reported.[9,19]